Flash spark plasma sintering of zirconia nanoparticles: Electro-thermal-mechanical-microstructural simulation and scalability solutions

Charles Manière, Christelle Harnois, Guillaume Riquet, Jérôme Lecourt, Christelle Bilot, Sylvain Marinel

Flash spark plasma sintering of zirconia nanoparticles: electro-thermal-mechanical-microstructural simulation and scalability solutions

Charles Manière[1]*, Christelle Harnois[1], Guillaume Riquet[1], Jérôme Lecourt[1], Christelle Bilot[1], Sylvain Marinel[1]

1. Normandie Univ, ENSICAEN, UNICAEN, CNRS, CRISMAT, 14000, Caen, France

Keywords

Flash sintering; zirconia; simulation; scalability; spark plasma sintering

Abstract

Flash sintering is a very promising method with a great potential for the ultra-rapid production of objects with firing processes of mere seconds. However, the transition from few millimeters samples to larger scales is a key issue. In this study, we explore the spark plasma sintering approach allowing a stable hybrid heating in flash condition and producing near net shape sintered specimens. Two electric current configurations are employed for diameters of 15 and 30 mm to determine the effect of scale change and of electric current concentration. These experiments coupled with a Multiphysics simulation indicate that stable flash conditions can be reached for 30 mm specimens. However, even if the electrical current concentration is very effective at small sizes, it generates peripheral hot spots for large specimen dimensions. The blackening effect on zirconia flash specimens acts then as an indicator of the specimen thermal history.

Graphical Abstract

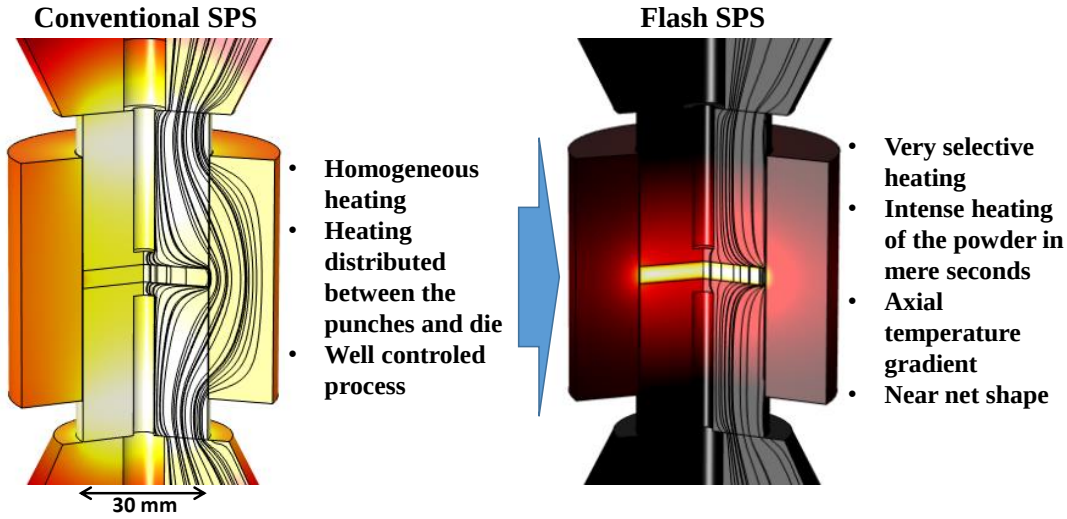

* Corresponding author: **CM**: Laboratoire de cristallographie et sciences des matériaux (CRISMAT), 6 Bvd du maréchal Juin 14050 CAEN CEDEX 4, France

Ph.: +33.2.31.45.13.69 ; *E-mail address*: charles.maniere@ensicaen.fr

Nomenclature

θ Porosity

$\dot{\theta}$ Porosity elimination rate (s^{-1})

$\underline{\sigma}$ Stress tensor ($N.m^{-2}$)

σ_{eq} Equivalent stress ($N.m^{-2}$)

$\underline{\dot{\varepsilon}}$ Strain rate tensor (s^{-1})

$\dot{\varepsilon}_{eq}$ Equivalent strain rate (s^{-1})

n Creep law stress exponent

A Creep law deformability term ($s^{-1}Pa^{-n}$)

A_0 Creep pre-exponential factor ($Ks^{-1}Pa^{-n}$)

m Creep law grain size sensibility exponent

Q Sintering activation energy ($J.mol^{-1}$)

R Gas constant 8.314 ($J.mol^{-1}.K^{-1}$)

T Temperature (K)

φ Shear modulus

ψ Bulk modulus

Pl Sintering stress (Pa)

$\mathbb{i}$ Identity tensor

$\dot{e}$ Trace of the strain rate tensor (s^{-1})

$\dot{\gamma}$ Shear strain rate invariant (s^{-1})

I_1 Trace of the stress tensor ($N.m^{-2}$)

$\dot{G}$ Grain growth rate ($m.s^{-1}$)

G Grain size (m)

G_0 Initial grain size (m)

p Grain growth equation grain size exponent

K Grain growth factor ($m^{1+p}.s^{-1}$)

k_0 Grain growth pre-exponential factor ($m^{1+p}.s^{-1}$)

Q_G Grain growth activation energy ($J.mol^{-1}$)

SPS Spark Plasma Sintering

ETMM Electro-Thermal-Mechanical-Microstructural

$\vec{J}$ Electric current density ($A\ m^{-2}$)

$\vec{E}$ Electric field ($V\ m^{-1}$)

$\boldsymbol{J}$ Electric current density norm ($A\ m^{-2}$)

$\boldsymbol{E}$ Electric field norm ($V\ m^{-1}$)

σ_{elec} Electric conductivity ($S\ m^{-1}$)

ρ Density (kg m^{-3})

C_p Heat capacity (J kg^{-1} K^{-1})

T Temperature (K)

κ Thermal conductivity (W m^{-1} K^{-1})

φ_{conv} Convective heat flux (W m^{-2})

h_{conv} Convective heat flux coefficient (W m^{-2} K^{-1})

T_{water} Water temperature (300 K)

T_{solid} Calculated solid temperature (K)

J_{rad} Surface radiosity (W m^{-2})

σ_s Stefan Boltzmann constant (5.67E-8 W m^{-2} K^{-4})

ϵ Emissivity

$\boldsymbol{G}$ Thermal irradiation flux (W m^{-2})

Nr Refractive index

$e_b(T)$ Surface radiation produced (W m^{-2})

$refl$ Reflected radiative heat flux (W m^{-2})

φ_{rss} Net inward radiative heat flux (W m^{-2})

$\vec{n}$ Normal unit vector

J_n Imposed normal electric current density (A m^{-2})

J_c Contact current density (A m^{-2})

ECR Electric surface contact resistance (Ω m^2)

U_i Contact i face electric potential (V)

$\dot{q}_c$ Contact heat flux (W m^{-2})

TCR Thermal surface contact resistance (m^2 K W^{-1})

T_i Contact i face temperature (K)

α Coefficient of thermal expansion (T^{-1})

1. Introduction

Since the discovery of flash sintering in 2010[1,2], many efforts have been employed to study the underlying heating/sintering mechanisms and to scale up this ultra-rapid process[3–5]. The flash sintering involves an abrupt heat dissipation followed by the sintering of the specimen in mere seconds. For zirconia, this "flash event" is mostly initiated by the NTC (negative temperature coefficient) resistivity of this material generating an incubation stage and an abrupt current flowing in the ceramic at high temperature[6]. The ultra-rapid sintering kinetics are generally not explained by the heating speed that would require higher temperatures and suggest additional mass transport mechanism or kinetic mechanisms[1,7]. Concerning the non-thermal mass transport mechanisms, we can cite the current effects (electromigration[8,9], electroplasticity[10–12], Frenkel pair cascade[7]) and the field effects (for instance, the ponderomative forces[13–15]). Concerning the thermal/kinetics effects, we can cite the localized heating[7,16,17], the high heating rate effect on delayed pore surface diffusion [18,19]. We may also cite the non-equilibrium state of grain boundaries[20,21] and grain boundary complexion[22,23]. The origin of the flash sintering ultra-rapid mechanism is still under hard debate[24,25]. It must bear in mind that the high thermal instability of flash sintering makes the estimation of the effective temperature very difficult due to the presence of hot spots and temperatures gradients[3,26,27]. It is then difficult to separate the thermal and non-thermal effects.

In flash sintering, the cooling flux generates thermal gradient at the edges of the specimen[28]. The NTC behavior tends to amplify these thermal gradients by a higher volumetric dissipation in the hot area where the current tends to concentrate[29,30]. For materials having low thermal conductivity like zirconia, this phenomenon is even more amplified and hot spots may appear. Dong [31] has expressed this in a figure of merit based on thermal relaxation theory. In microwave sintering, the hot spot formation is typically observed in the case of the direct heating of zirconia[29]. The latter is initiated by cooling

fluxes by conduction, convection and radiation at the edge[28]. The finite element simulation helps in predicting and quantifying these fluxes. For SPS[32], the cooling fluxes at the specimen boundaries are only caused by the conduction through the surrounding graphite elements acting as susceptors in direct contact. The thermal gradients are strongly influenced by the electrical and thermal contacts which play a similar role are thermal barrier and dissipate heat at the boundaries[33–36]. These hybrid heating characteristics concentrate the heat in the powder making flash SPS more stable and more controllable than the conventional resistive approach. In addition, the punches and die allow controlling the external shape of the flashed specimen.

Different flash SPS approaches have been developed. The first is based on a sinter-forging configuration where a graphite felt or foil is used to initiate the heating. Zirconia[37], ZrB_2[38], SiC[39–42], Nd-Fe-B[43], TiB_2-*h*BN[44], B_4C[45] materials have been produced by this method. This method is very interesting for achieving high density of refractories as the radial shrinkage allows the pore flattening and porosity elimination during the sinter-forging SPS approach[46,47]. High dimension specimens have been produced by this method[39]. Another approach uses a graphite die to control the final shape of the sample. The graphite die is generally electrically insulated by a boron nitride spray to concentrate the electrical current in the powder and the graphite foil which initiate the heating and act as a susceptor. This configuration has been used to sinter ZrB_2, $MoSi_2$, Al_2O_3[48], SiC[49]. In a previous study[50], it was shown that this configuration provides an electro-thermal-mechanical confinement to the powdered specimen that can be ultra-rapidly heated and sintered with very controllable and homogeneous conditions. In the latter, we showed that these ultra-rapid conditions allowed the sintering of almost all materials from dielectrics, semiconductors to metals. These experiments were done on alumina, zirconia and nickel and for 10 mm diameter samples. However, the preservation of these stable ultra-rapid conditions for bigger samples is still questionable.

In this work, the scalability of flash SPS of zirconia is tested for cylindrical samples with diameter ranging from 15 to 30 mm. The flash sintering is investigated in different configurations of electrical current to identify stable heating/sintering conditions. A fully coupled electro-thermal-mechanical-microstructural simulation of the different tests is conducted to model the temperature, porosity and grain size fields of each flash test.

2. Theory and calculations

2.1 Electro-Thermal-Mechanical-Microstructural model (ETMM Model)

The ETMM simulation of spark plasma sintering includes the coupled Joule heating and sintering governing equations. The Joule heating obeys the charge conservation and heat transfer equations.

$$\nabla.\vec{J} = \nabla.\left(\sigma_{elec}\vec{E}\right) = 0 \quad (1)$$

$$\nabla.\left(-\kappa\nabla T\right) + \rho C_p \frac{dT}{dt} = \boldsymbol{JE} \quad (2)$$

Where $\boldsymbol{JE}$ is the volumetric electrical power dissipated.

The sintering part is simulated with the continuum theory of sintering [24,51,52]. The local momentum equation of the mechanical part is:

$$\nabla.\underline{\sigma} = 0 \quad (3).$$

The porous viscoplastic sintering behavior is defined by the strain rate and stress tensor relationship:

$$\underline{\sigma} = \frac{\sigma_{eq}}{\dot{\varepsilon}_{eq}}\left(\varphi\underline{\dot{\varepsilon}} + \left(\psi - \frac{1}{3}\varphi\right) tr\left(\underline{\dot{\varepsilon}}\right)\mathbb{i}\right) + Pl\mathbb{i} \quad (4).$$

The expression of the shear φ and bulk ψ moduli (porosity functions) can be theoretically approximated [51,53]. However, a SPS-based experimental identification method has been developed [54–56]. For the ceramics the independent identification of the moduli and creep parameters is very challenging due to the grain growth disturbances on the creep behavior at the final stage. A method allowing the direct identification of both the creep and moduli

directly from porous stage with tests like sinter-forging has been developed[57]. Below, moduli and creep law was obtained for the zirconia powder employed in this study:

$$\varphi = \left(1 - \frac{\theta}{0.6}\right)^{3.4} \quad (5)$$

$$\psi = 0.07\,\frac{(1-\theta)^{5.8}}{\theta} \quad (6)$$

$$\dot{\varepsilon}_{eq} = \frac{1.34E3[Pa^{-2}s^{-1}K]}{T}\left(\frac{G_0}{G}\right)^{m} \exp\left(\frac{-536[kJ\,mol^{-1}]}{RT}\right)\sigma_{eq}{}^{2} \quad (7)$$

with the expressions:

$$\dot{\varepsilon}_{eq} = \frac{1}{\sqrt{1-\theta}}\sqrt{\varphi\dot{\gamma}^2 + \psi\dot{e}^2} \quad (8)$$

and the strain rate tensor invariants:

$$\dot{e} = \dot{\varepsilon}_x + \dot{\varepsilon}_y + \dot{\varepsilon}_z \quad (9)$$

$$\dot{\gamma} = \sqrt{2\left(\dot{\varepsilon}_{xy}^2 + \dot{\varepsilon}_{xz}^2 + \dot{\varepsilon}_{yz}^2\right) + \frac{2}{3}\left(\dot{\varepsilon}_x^2 + \dot{\varepsilon}_y^2 + \dot{\varepsilon}_z^2\right) - \frac{2}{3}\left(\dot{\varepsilon}_x\dot{\varepsilon}_y + \dot{\varepsilon}_x\dot{\varepsilon}_z + \dot{\varepsilon}_y\dot{\varepsilon}_z\right)} \quad (10).$$

The volume change rate is related to the porosity elimination rate by the mass conservation equation:

$$\frac{\dot{\theta}}{(1-\theta)} = \dot{\varepsilon}_x + \dot{\varepsilon}_y + \dot{\varepsilon}_z \quad (11).$$

The grain growth is modeled by the following rate equation.

$$\dot{\mathrm{G}} = \frac{K(T)}{G^p} \quad (12)$$

$$K(T) = K_0 \exp\left(\frac{-Q_G}{RT}\right) \quad (13)$$

2.2 Boundary and interface conditions

The electro-thermal boundary conditions and mesh of the SPS column are represented in figure 1. An anisotropic mesh is employed to have three elements in the 0.2 mm thickness of the graphite foil where the electrical current is concentrated in flash conditions. The electrode water cooling is modeled by a convective flux [34,58,59] with the following equation:

$$\varphi_{conv} = h_{conv}(T_{water} - T_{solid}) \quad (14).$$

The graphite surfaces radiate towards each other and metallic adjacent surfaces of the SPS are maintained at room temperature. The heat loss by radiation is calculated by the surface to surface radiation module of comsol defining the radiosity flux J_{rad} as the sum of the surface thermal radiation $\epsilon e_b(T)$ and the reflected part (*refl*) of the incident flux $\boldsymbol{G}$.

$$J_{rad} = refl + \epsilon e_b(T) = (1-\epsilon)\boldsymbol{G} + \epsilon(Nr)^2\sigma_s T^4 \quad (15).$$

For a surface, the net inward heat flux φ_{rss} is defined by:

$$\varphi_{rss} = \epsilon(\boldsymbol{G} - e_b(T)) \quad (16).$$

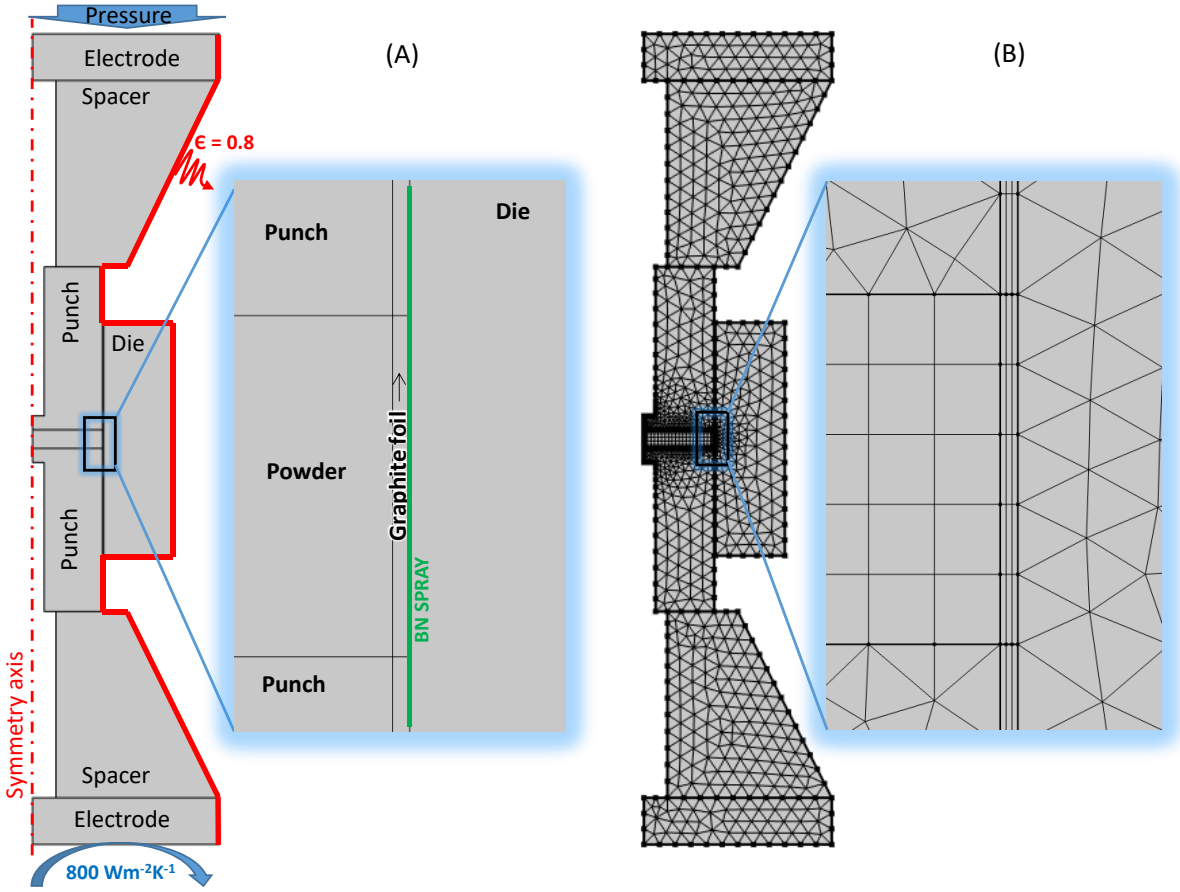

Figure 1 Flash SPS configuration, (a) 30 mm samples configuration and model boundary condition (b) mesh.

A graphite emissivity of 0.8 is chosen [33]. The natural convection [60,61] is neglected since the cavity is under vacuum. The electric boundary conditions are the following: the ground is located at the lower electrode, a numerical PID is incorporated [62] at the upper electrode *via* a normal current density J_n and electrical insulations are considered for all other surfaces $J_n = 0$:

$$-\vec{n}.\vec{J} = J_n \quad (17)$$

The electric and thermal contact resistances (ECR and TCR) have a high influence on the thermal field [34,35,63–65] and obey:

$$J_c = \frac{1}{ECR}(U_1 - U_2) \quad (18)$$

$$\dot{q}_c = \frac{1}{TCR}(T_1 - T_2) \quad (19).$$

The ECR TCR and temperature-dependent electro-thermal properties have been taken from [33] and [66]. The electrical conductivity of zirconia has been taken from [67] where flash sintering was applied with an alumina die without graphite foil, allowing to get an estimation of the zirconia resistivity under vacuum conditions at high temperatures. In the calculation, the boron nitride spray interfaces are assumed to be electrically insulating. All the material properties are gathered in the appendix.

3. Experiment and method

All experiments have been conducted on the SPS apparatus "FCT HPD25" with the graphite grade mersen 2333. A 40 nm yttria stabilized zirconia nano-powder (Tosoh TZ-3Y-E) is employed for this study. Two tooling geometries are employed. The geometry of the 30 mm sample diameter tests is reported in figure 1a. For the 15 mm tests, the heights of the punches and die are similar and the die diameter is reduced to 45 mm. The sintering sample height is 2 mm for all experiments, 2 and 8 g of powder are taken for the 15 and 30 mm tests, respectively. Two electrical current configurations are used: one conventional (called "die heating") where the current can flow through the punches, graphite foil, die and another referred as "concentrated" where the die is electrically insulated by a boron nitride spray (figure 1a) to concentrate the current in the powder and the graphite foil acting as a susceptor (called "concentrated" configuration). In order to complete this explorative design, two thermal cycles were imposed to the punch temperature, one typical with a 100 K/min ramp and another at 1000 K/min to impose flash but controlled conditions. A dwell is programmed

at 1400 °C but the test is manually stopped when the displacement indicates the end of the sintering process. The powder quantity is calculated for 2 mm thick sintered samples. The experimental design includes 8 tests with the combinations of the three following parameters: of the specimen diameter (Ø15, Ø30, scalability), heating rate (100, 1000 K/min) and electric current configurations ("die heating", "concentrated"). The samples relative density was measured by Archimedes's method and the average grain size was determined on polished surfaces using the linear intercept method with Mendelson's stereological factor (1.56) [68]. An ETMM simulation of each of these tests has been conducted to describe the differences in the Multiphysics fields (temperature, porosity, grain size, etc.). The calculations have been done *via* the simulation software COMSOL Multiphysics® with the heat transfer module for the surface to surface radiation and electro-thermal contact resistance and the nonlinear material module to implement manually the sintering physics. The obtained microstructures have been analyzed by SEM on polished cross-section surfaces.

4. Results and discussions

4.1. ETMM simulation calibration

The simulation study started by conducting a calibration of the thermal field (with in particular the lateral contact resistance which differs from [33,66]). Once the ECR, TCR have been adjusted with the punch/die pyrometers, the grain growth and the creep grain size exponent m were adjusted to correspond to the final relative density and grain size for all tests. As said earlier, the moduli and creep behavior was determined previously [57]. The latter employed electrically insulated and isothermal conditions at the porous stage. The following values were obtained $k_0 = 0.04\ m^{1+p}.s^{-1}$, $Q_G = 575$ kJ/mol, $p = 1.63$ (from [69]) and $m = 2$. The graphite/foil/graphite ECR and TCR formulas obtained are $3.11E^{-7}\exp(-2.61E^{-3}T)\ \Omega m^2$ and $1.79E^{-3}\exp(-1.53E^{-3}T)\ m^2KW^{-1}$ respectively. The outcome of this calibration is

shown in figure 2 where the ETMM simulation was conducted and compared to the experimental values for the test Ø30 mm, 100 K/min, in "die heating" current configuration.

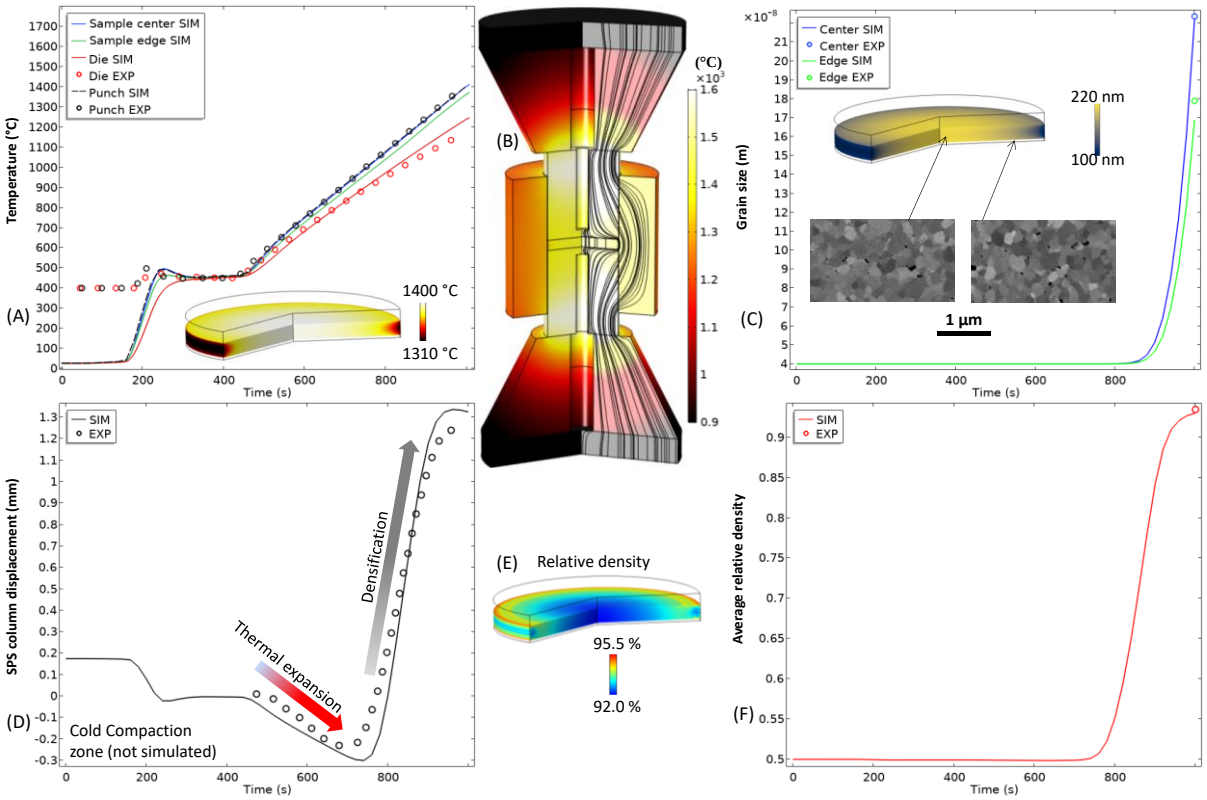

Figure 2 Calibration/verification of the electro-thermal-mechanical-microstructural simulation: (a) temperature curves, (b) temperature field of the SPS column, (c) grain size, (d) displacement, (e) specimen final relative density field, (f) simulated average relative density curve.

4.2. SPS tests curves

The punch temperature, SPS displacement, RMS current (I_{rms}) and voltage (U_{rms}) curves are reported in figure 3 for the 30 mm diameter tests. These curves allow comparing the heating/sintering response of the four configurations for current distribution and heating rate. The curves in figure 3a show the typical response of a SPS test at 100 K/min with linear I_{rms}, U_{rms} curves and apparent sintering temperatures taking place between 1000 and 1400 °C. In the same electric current configuration at 1000 K/min, abrupt current/voltage curves are observed with an overshot of the temperature and a quick stabilization to similar apparent sintering temperatures. If the "concentrated" configuration of electrical current is employed (BN spray), the test at 100 K/min (figure 3c) shows a non-linear current profile compared to the equivalent die heating test (figure 3a). At 1000 K/min (figure 3d) an abrupt current profile

without stabilization is observed while the sintering duration is 30 sec between 800 and 1400°C of apparent temperatures. This behavior of the temperature, current/voltage experimental curves is similar to the 15 mm tests.

In order to compare the behavior of the apparent sintering response to all tests, the displacement curves are plotted *vs* the apparent temperature in figure 4a. When using the concentrated configuration, the sintering zones take place about 150 K lower than it does with the die heating method. For the 15 mm diameter tests, the curves at 1000 K/min are systematically shifted toward higher temperatures. For the 30 mm diameter tests, this shift is smaller for the “die heating” configuration and inverted for the “concentrated” configuration where slightly lower sintering temperature is observed for the highest heating rate. These observations suggest a significant temperature difference between the apparent punch temperature and the effective powder temperature. In the next section, the ETMM simulations of all the 8 tests are fully disclosed to describe the internal fields and their differences.

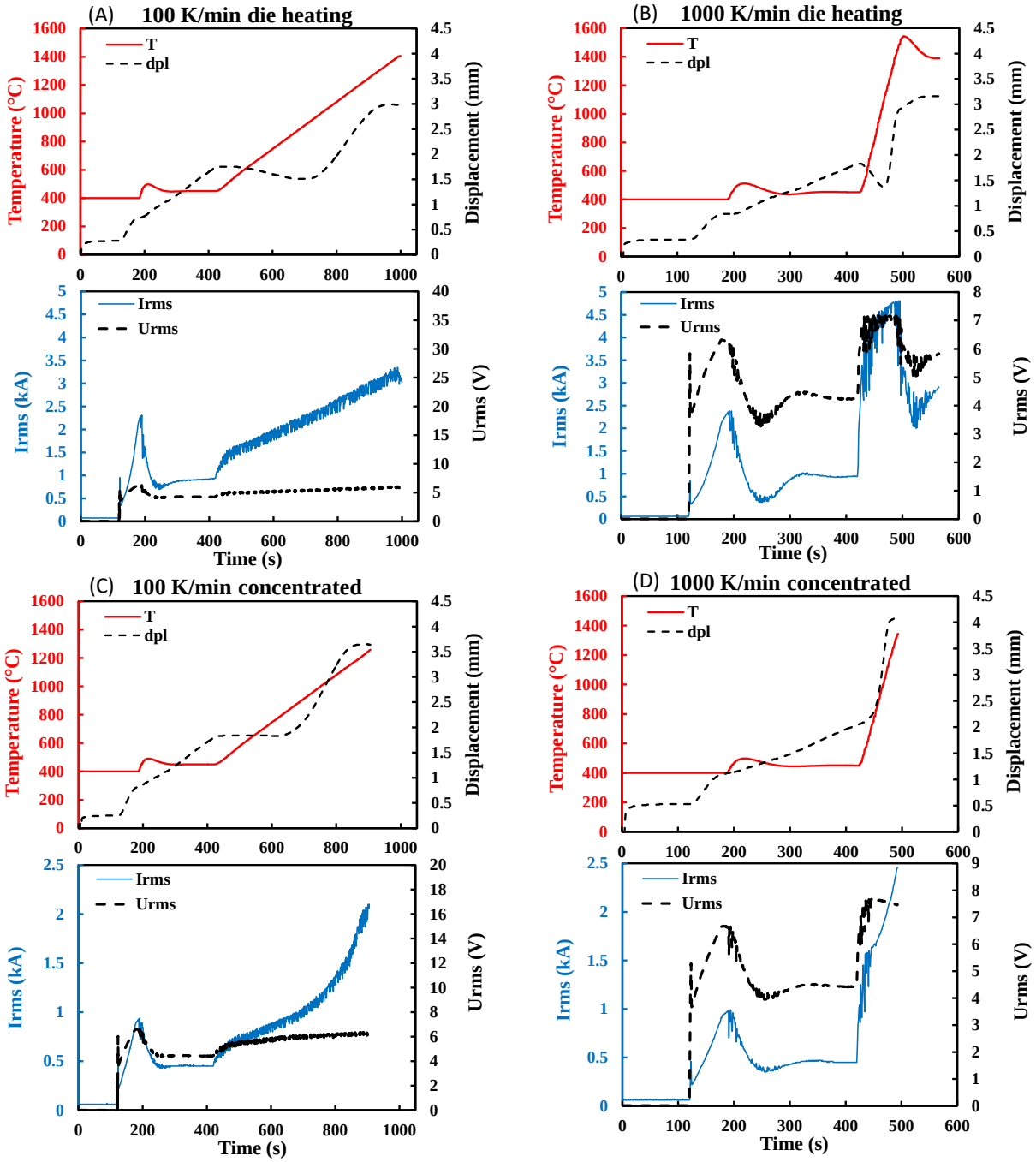

Figure 3 Temperature, displacement, rms current and voltage experimental data for the 30 mm tests, (a) die heating configuration 100 K/min, (b) die heating configuration 1000 K/min, (c) electric current concentration configuration (concentrated configuration) at 100 K/min, (d) electric current concentration configuration at 1000 K/min.

In figure 4b, the simulated average relative density curves are plotted *vs* time to compare the expected sintering duration and compare the final relative density with the experimental data. In overall, the model fits well all final relative densities (error less than 5 %). These curves indicate a densification rate of about 20 %/min for 100 K/min and 130 %/min for

1000 K/min for sintering duration of about 250 sec, and 30 sec, respectively. These curves also show the impact of the grain growth on the slowing down of the densification curves due to equation (7).

The very interesting aspect of these curves (figure 4b) is that ultra-rapid sintering rates could be obtained without modifying the sintering model parameters identified at the same applied pressure and in isothermal and electrically insulated conditions in ref[57]. To carefully describe this, the simulated temperatures disclosed in the next section must be discussed as well. This suggests experimentally that the measured moduli at porous stage give a better description of the true porous skeleton (with pore shape different than spherical pores). This suggests a high sintering reactivity of powders under flash conditions.

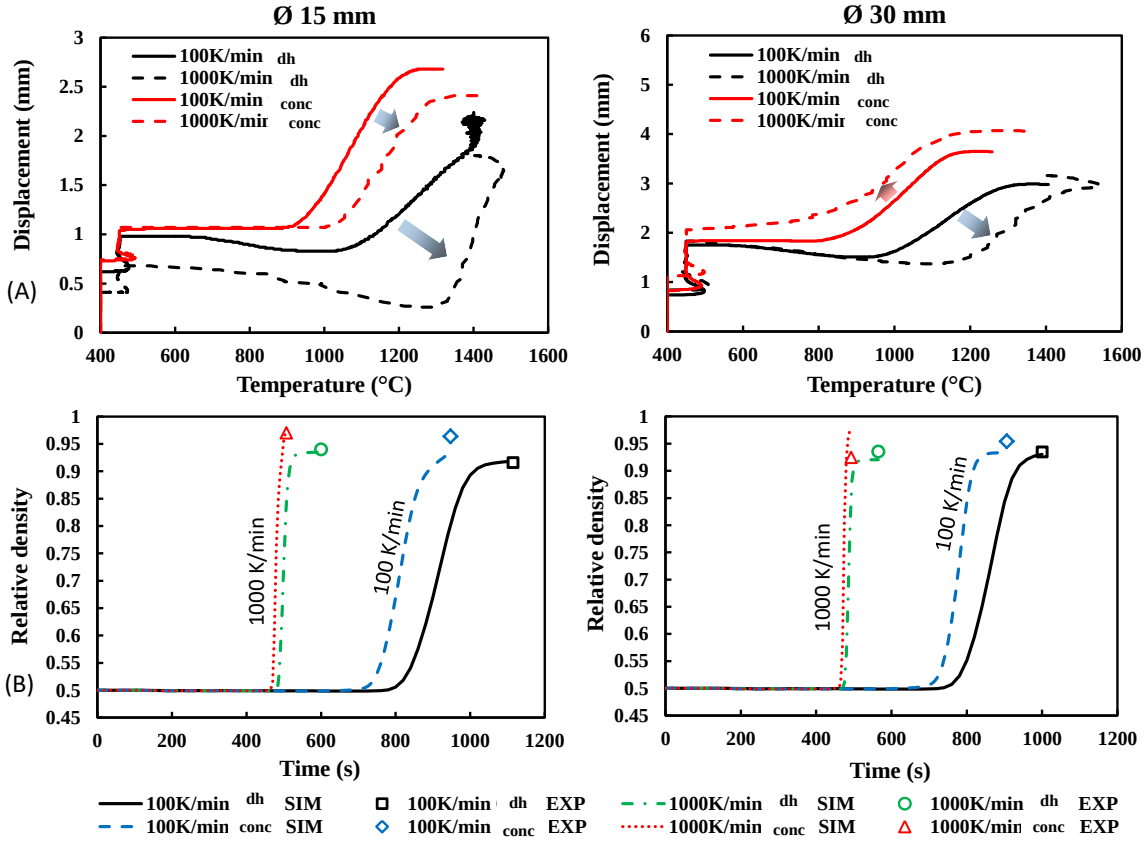

Figure 4 (a) Displacement and (b) simulated relative density curves, "dh" and "conc" refer to the "die heating" and "concentrated" configurations respectively.

4.3. Electro-thermal-mechanical-microstructural simulation of the concentrated / die heating configurations

In this section, the ETMM simulations of all the tests are displayed and compared to each other. Each figure compares the experimental/simulated temperature curves in the punch/die and in the sample, the SPS column simulated temperature field at the end of the heating (the minimum temperature scale is fixed at 900 °C) and the temperature, grain size, relative density of the sample at the end of the cycle.

The 15 mm diameter tests in “die heating” electrical current configuration are reported in figure 5. The heating is concentrated in the punches where a temperature of 1900 °C is observed. In the sample, the temperature is distributed from 1600 °C in the center to 1540 °C at the edge where lower grain size and densification are observed. At 1000 K/min, the temperatures/grain sizes are very similar and despite the high heating rate, the densification is close to the one observed on the 100 K/min test. The sintering seems to follow the high heating rates. An overshoot with temperatures 150 K higher is observed for the test at 1000 K/min.

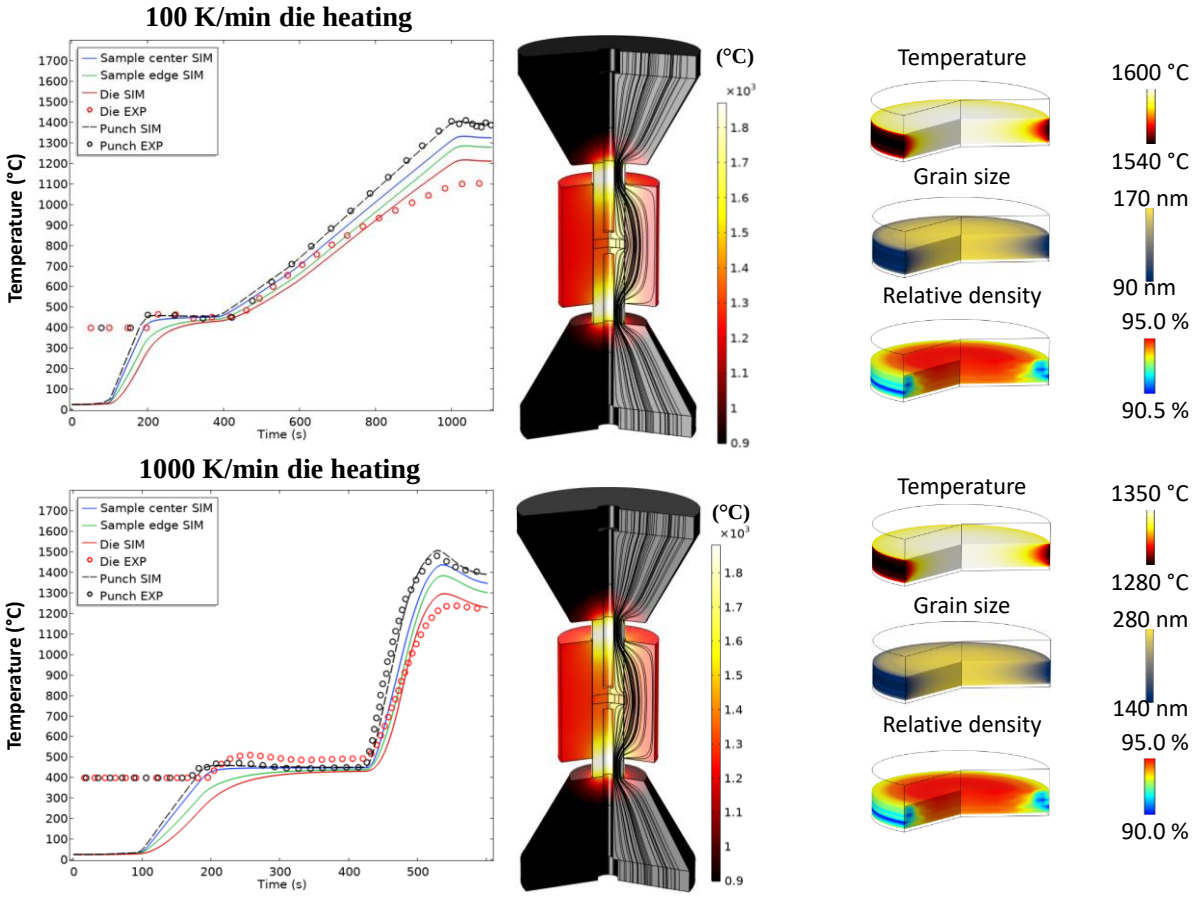

Figure 5 Simulated ETMM model of the 15 mm diameter specimens in die heating configuration at 100 K/min and 1000 K/min.

The 15 mm diameter tests in “concentrated” electrical current configuration are reported in figure 6. The temperature distribution is very different from the “die heating” configuration. Is this case, the electrical current is highly concentrated in the powder/graphite and foil/die interface at low temperatures where the zirconia powder behaves practically like a dielectric. At high temperatures, the zirconia powder becomes conductive and the current lines are distributed between the powder and graphite foil. A significant heat is then dissipated and confined in the powder zone. The specimen temperature has a vertical gradient with cooler temperatures near the contact zone with the punches, and higher temperatures, grain sizes and relative density near the center. Because of this significant heat concentration in the sample, the apparent temperature measured in the punches is 200 K lower than the sample. At 1000 K/min, the latter is increased to 500 K at the end. The temperature distribution is relatively close to the 100 K/min test but the thermal confinement is bigger due to the significant reduction of time for the heat to diffuse from the specimen zone to nearby graphite tooling.

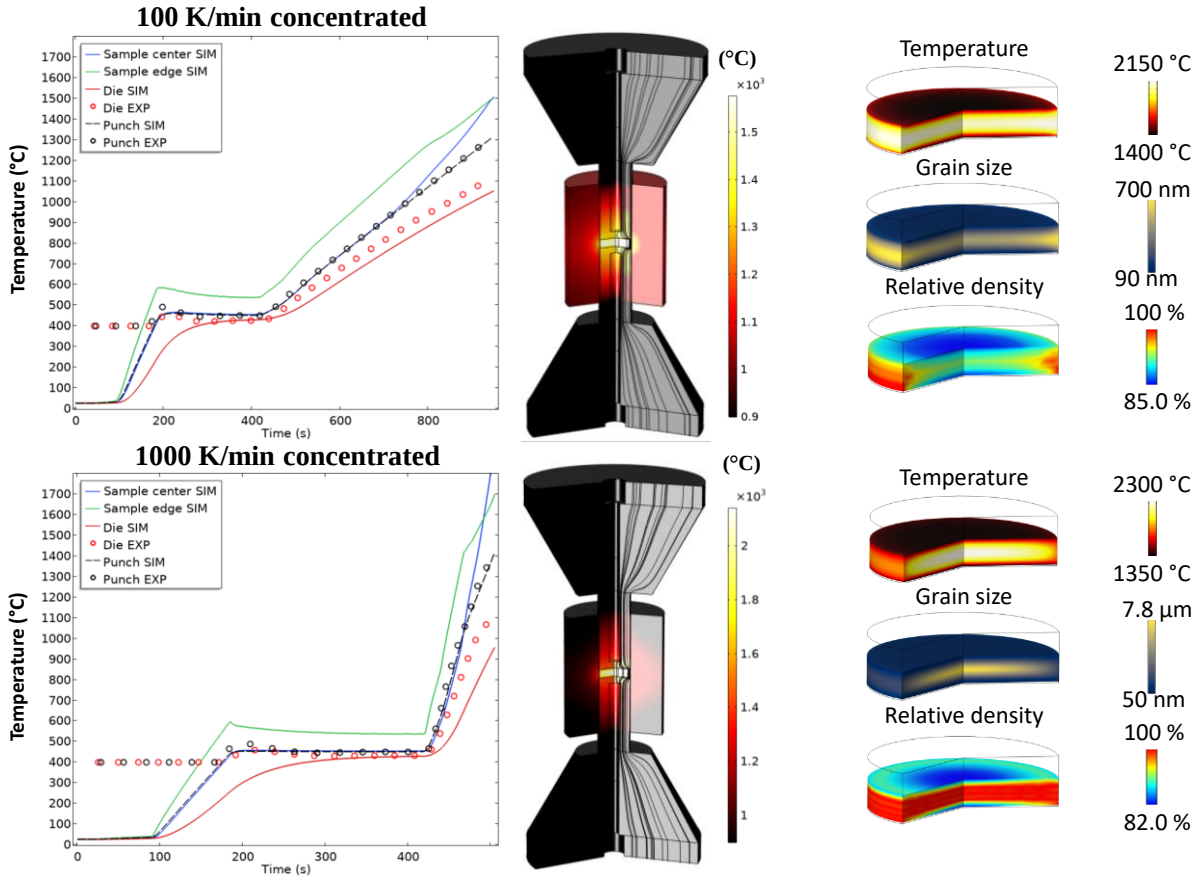

Figure 6 Simulated ETMM model of the 15 mm diameter specimens in "concentrated" configuration at 100 K/min and 1000 K/min.

The 30 mm diameter tests in "die heating" electrical current configuration are reported in figure 7. Compared to the equivalent case at 15 mm diameter (figure 5), the heat concentration in punches is less pronounced due to the larger section of the punches and the heat is more homogeneously distributed is the punches/sample/die zone. Nevertheless, the specimen fields have a very similar distribution compared to the 15 mm tests in "die heating" configuration. At 1000 K/min, a 200 K overshot is observed similarly to the equivalent test at 15 mm diameter.

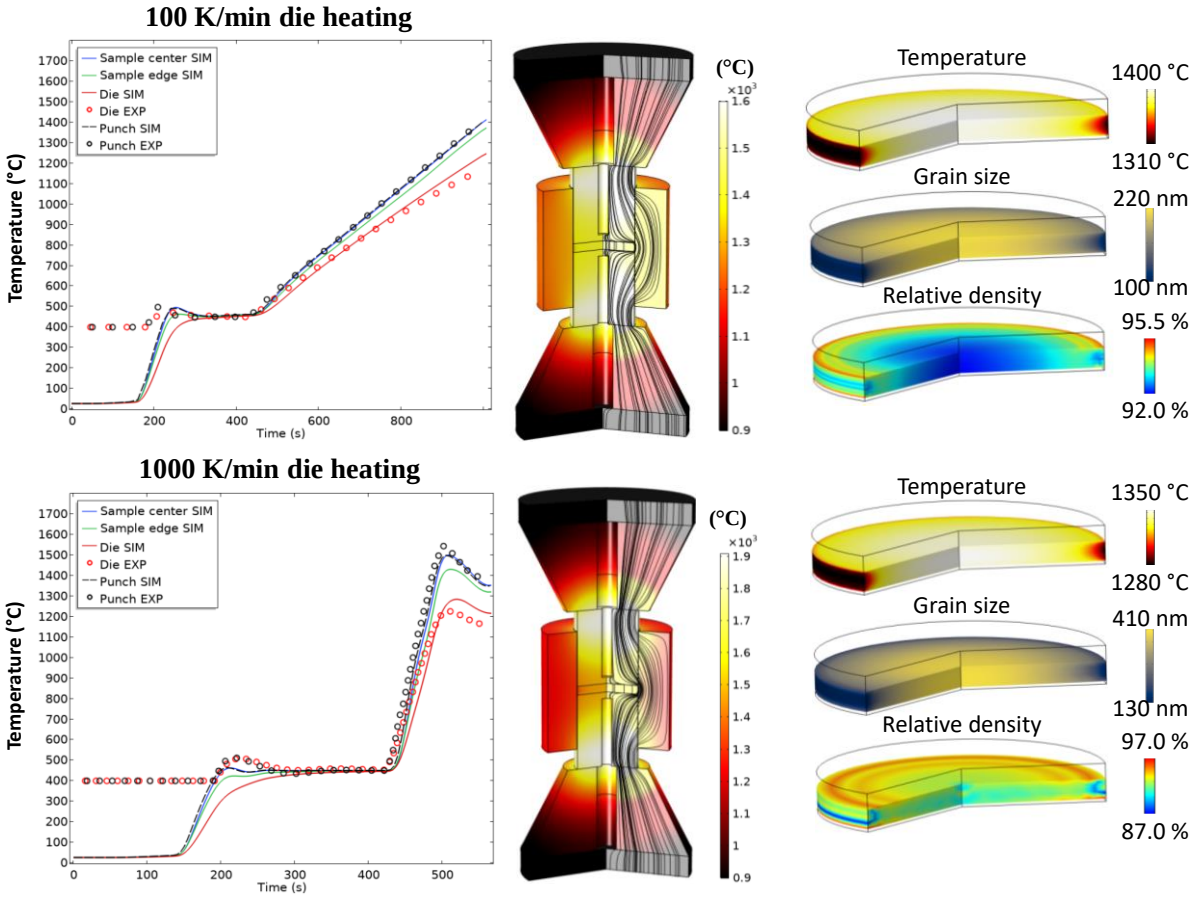

Figure 7 Simulated ETMM model of the 30 mm diameter specimens in die heating configuration at 100 K/min and 1000 K/min.

The 30 mm diameter tests in “concentrated” electrical current configuration are reported in figure 8. The temperature field distribution from “die heating” to “concentrated” configuration in 30 mm diameter tests is very similar to the test at 15 mm. A significant heat concentration is still observed despite the flatter specimens shape at 30 mm. The axial thermal gradient behavior of the temperature/relative density/grain size fields is still observed. The differences between the apparent punches temperature and the specimen is of the same order as for the 15 mm sample diameter: 200 K and 500 K at 100 and 1000 K/min respectively. In the next section, these results are compared to the experimental microstructures.

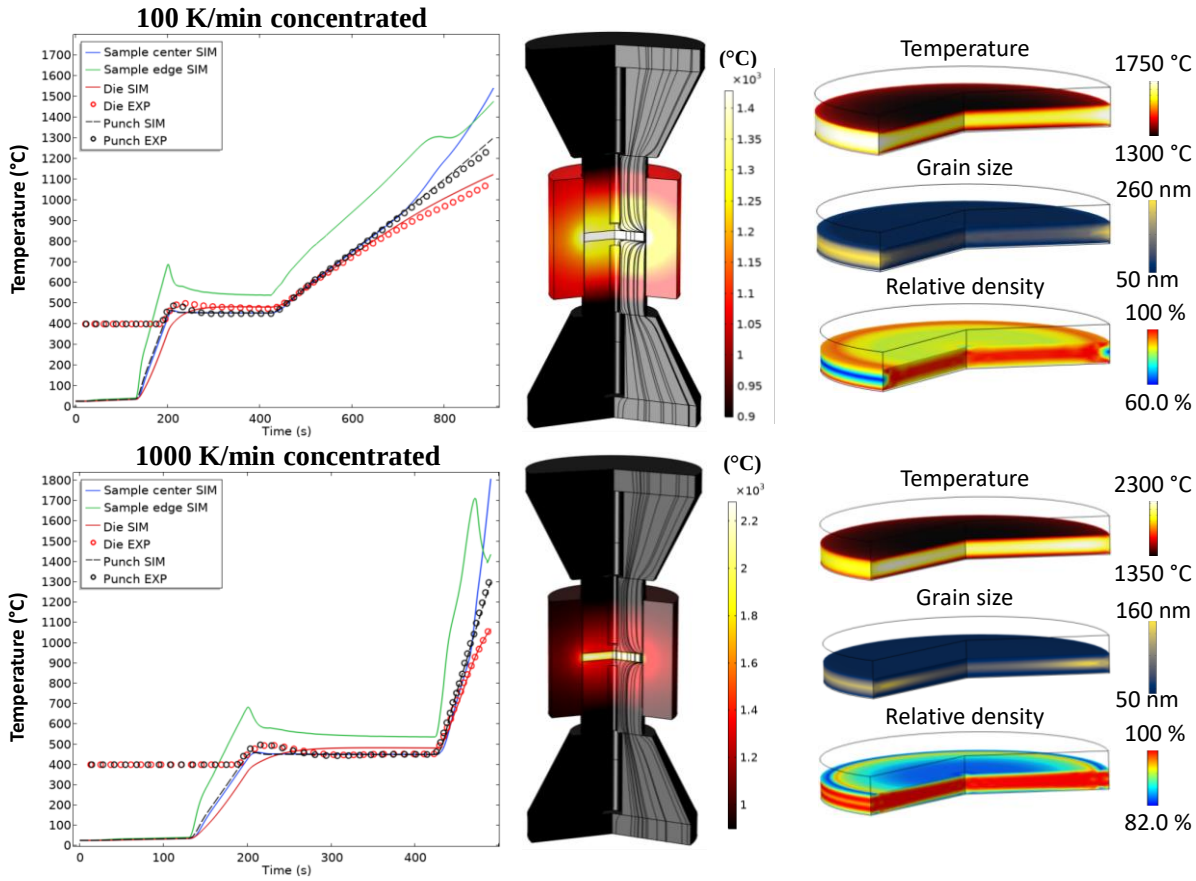

Figure 8 Simulated ETMM model of the 30 mm diameter specimens in "concentrated" configuration at 100 K/min and 1000 K/min.

4.4. Microstructure analysis

The microstructures of all the 15 and 30 mm diameter tests are reported in figure 9. To investigate the microstructure homogeneity and the effects of the Multiphysics field gradients, the microstructure was analyzed in the center and at the edge of the specimens. We can see that the microstructure homogeneity is very satisfactory for all tests in terms of porosity and grain size. The only exception concerns the 30 mm, 1000 K/min, "concentrated" test where an important grain size and porosity gradient are observed near the edge. In the corresponding simulation in figure 8, the radial grain size gradient is observed but the relative density distribution should be axially distributed. In the photograph of this test a complex distribution of blackened zone is observed in the zirconia cross-section. This blackening phenomenon follows the simulated specimen current density distribution reported below in figure 9, it

points out a hot spot near the edge. In particular, a thin black zone is present at mid height. A similar distribution has been observed by simulation the Peltier effect in SPS of colusite sulfur thermoelectric specimens [70]. The latter generates local temperature maximums by the coupling of the thermoelectric flux [66] and the thermal contact resistance. However, without the information of the Seebeck coefficient at such high temperatures for zirconia, it is difficult to conclude on the origin of this phenomenon. A competition between the reduction front and the pollution species diffusion may also be present.

Concerning the blackening effect on zirconia samples, the aspect of each sintered sample was described in figure 9. Comparing these aspects to the simulated temperatures, this effect seems to appear for the high temperatures > 1500 °C and preferentially during the "concentrated" configurations where the concentration of the electrical current in the powder seems to accelerate the reduction phenomena. The blackening effect is well known is the zirconia flash sintering, it is associated with a reduction phenomenon appearing near the electrodes and propagating through the other[72,73]. The latter is often accompanied by a significant rise of the electrical conductivity switching from ionic conduction to electronic conduction. For SPS imposing reductive conditions, this effect may be accelerated.

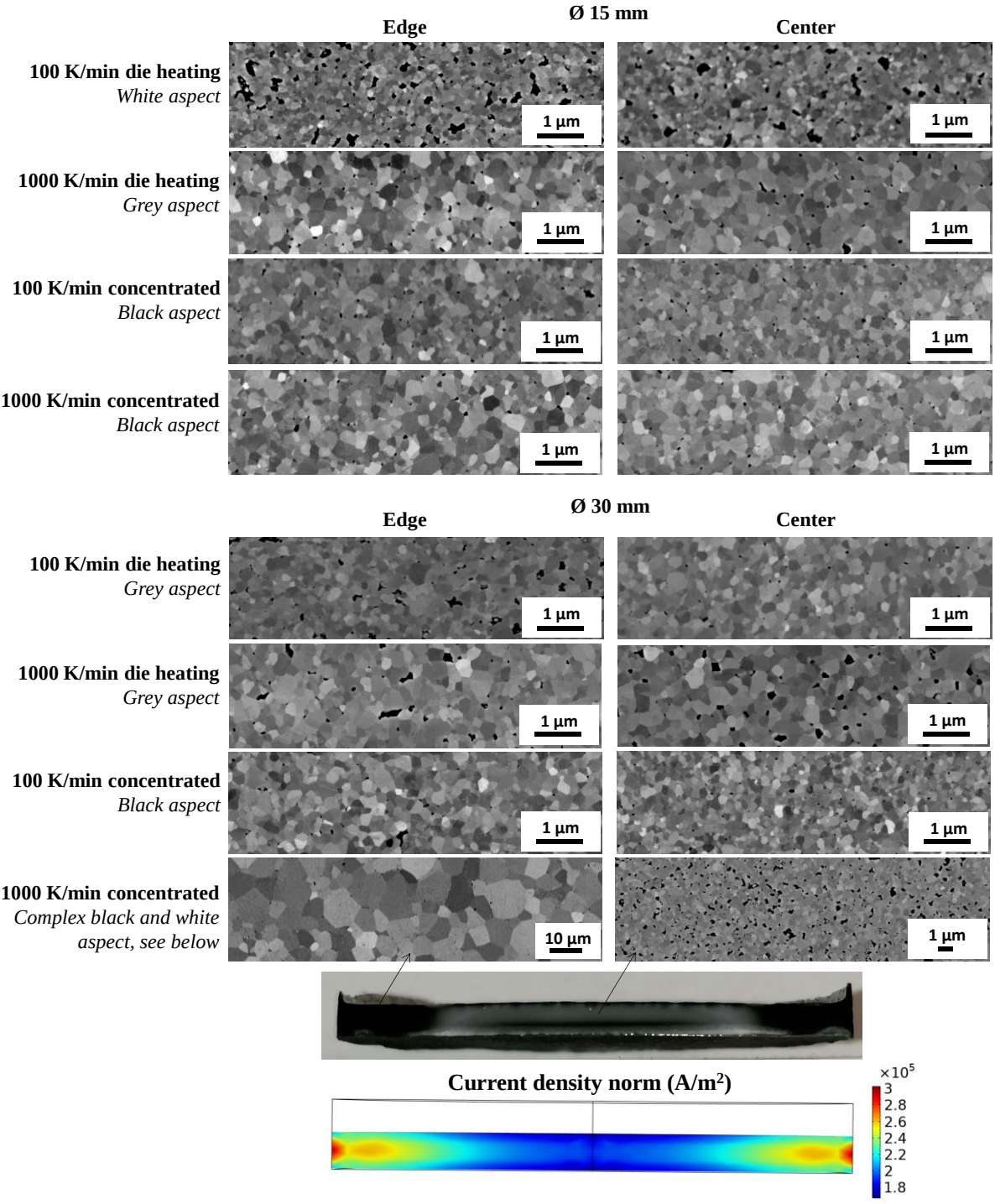

Figure 9 Polished SEM microstructures of the specimens at 100 K/min, 1000 K/min and for the "die heating" and "concentrated" electrical current configurations.

5. Conclusion

In this study, the flash spark plasma sintering of zirconia is investigated from medium to large size samples. The exploration consisted of comparing the typical SPS configuration in electric current distribution and heating rate (100 K/min) to ultra-rapid heating rates (1000 K/min) and concentrated electrical current configuration. The experiments and electro-thermal-mechanical-microstructural simulations of each case show that the thermal distribution of the 15 mm and 30 mm sizes are radial for a classic electrical current and becomes axial when the die is electrically insulated. Submicronic microstructures have been obtained with a good stability between the center and the edge. The exception is the 30 mm test in “concentrated” configuration showing intense grain growth and blackening effect at the edges. This shows the scalability limit of the “concentrated” configuration where the die is electrically insulated. Processing ultra-rapid heating over 15 mm specimens requires distributing the current in the die to avoid excessive overheating in the graphite foil during the preheating.

The thermal-sintering model shows that the sintering follows the high heating rates to sintering time down to 30 sec when 1000 K/min is employed. This suggests the need to use experimentally determined moduli which would help in predicting the high reactivity of the microstructures during ultra-rapid sintering.

Appendix

Table A Temperature dependent material properties of graphite, electrodes, and zirconia[33,62,74,75].

Materials		Expression
Graphite	*Cp* ($J.kg^{-1}.K^{-1}$)	$34.3+2.72.T-9.6E-4.T^2$
Electrode		446.5+0.162.T
Zirconia		$(43+2.35.T-4.34E-3.T^2+4.25E-6.T^3-2.09E-9.T^4+4.05E-13.T^5).\theta$
Graphite	κ ($W.m^{-1}.K^{-1}$)	$123-6.99E-2.T+1.55E-5.T^2$
Electrode		9.99+0.0175.T
Zirconia		(1.96-2.32E-4.T+6.33E-7.T2-1.91E-10.T3).(1-1.5θ)
Graphite	ρ ($kg.m^{-3}$)	1904-0.0141.T
Electrode		7900
Zirconia		$(6132-9.23E-2.T-7.26E-5.T^2+4.58E-8.T^3-1.31E-11.T^4).\theta$
Graphite	σ_{elec} (S/m)	$1/[1.70E-5-1.87E-8.T+1.26E-11.T^2-2.46E-15.T^3]$
Electrode		$1/[(50.2+0.0838.T-1.76E-5.T^2).1E-8]$
Zirconia		10509.exp(-11920/T).(1-1.5θ) 300-1200K (0.223.T-267).(1-1.5θ) 1200-1370K 5886.exp(-6894/T).(1-1.5θ)
Graphite	α (T^{-1})	$-1.25E-12.T^2+3.68E-9.T+1.33E-6$
Electrode		4.48E-9.T+1.09E-5
Zirconia		$-1.31E-12.T^2+3.98E-9.T+5.50E-6$

Acknowledgements

This study was funded by the French National Research Agency (ANR), project ULTRARAPIDE N°ANR-19-CE08-0033-01.

The help and support of Christophe Couder, Jérôme Lecourt and Christelle Bilot is gratefully acknowledged.

Data availability

The raw/processed data required to reproduce these findings cannot be shared at this time due to technical or time limitations.

Credit authorship contribution statement

Charles Manière: Conceptualization, Supervision, Modeling, Writing; **Christelle Harnois:** Conceptualization, Supervision, review & editing; **Guillaume Riquet:** Review & editing, **Christelle Bilot:** Characterizations, **Jérôme Lecourt:** Experimentation, **Sylvain Marinel:** Conceptualization, Supervision, review & editing.

References

[1] M. Cologna, B. Rashkova, R. Raj, Flash Sintering of Nanograin Zirconia in <5 s at 850°C, J. Am. Ceram. Soc. 93 (2010) 3556–3559. doi:10.1111/j.1551-2916.2010.04089.x.

[2] R. Raj, M. Cologna, A.L.G. Prette, V. Sglavo, Methods of flash sintering, Patent US 20130085055 A1, US 20130085055 A1, 2013. https://www.google.com/patents/US20130085055.

[3] M. Biesuz, V.M. Sglavo, Flash sintering of ceramics, J. Eur. Ceram. Soc. 39 (2019) 115–143. doi:10.1016/j.jeurceramsoc.2018.08.048.

[4] C.E.J. Dancer, Flash sintering of ceramic materials, Mater. Res. Express. 3 (2016) 102001. doi:10.1088/2053-1591/3/10/102001.

[5] M. Yu, S. Grasso, R. Mckinnon, T. Saunders, M.J. Reece, Review of flash sintering: materials, mechanisms and modelling, Adv. Appl. Ceram. 116 (2017) 24–60. doi:10.1080/17436753.2016.1251051.

[6] R.I. Todd, E. Zapata-Solvas, R.S. Bonilla, T. Sneddon, P.R. Wilshaw, Electrical characteristics of flash sintering: thermal runaway of Joule heating, J. Eur. Ceram. Soc. 35 (2015) 1865–1877. doi:10.1016/j.jeurceramsoc.2014.12.022.

[7] R. Raj, M. Cologna, J.S.C. Francis, Influence of Externally Imposed and Internally Generated Electrical Fields on Grain Growth, Diffusional Creep, Sintering and Related Phenomena in Ceramics, J. Am. Ceram. Soc. 94 (2011) 1941–1965. doi:10.1111/j.1551-2916.2011.04652.x.

[8] Z. Trzaska, J.-P. Monchoux, Electromigration experiments by spark plasma sintering in the silver–zinc system, J. Alloys Compd. 635 (2015) 142–149. doi:10.1016/j.jallcom.2015.02.122.

[9] E. Olevsky, L. Froyen, Constitutive modeling of spark-plasma sintering of conductive materials, Scr. Mater. 55 (2006) 1175–1178. doi:10.1016/j.scriptamat.2006.07.009.

[10] H. Conrad, Electroplasticity in metals and ceramics, Mater. Sci. Eng. A. 287 (2000) 276–287. doi:10.1016/S0921-5093(00)00786-3.

[11] G. Lee, C. Manière, J. McKittrick, E.A. Olevsky, Electric current effects in spark plasma sintering: From the evidence of physical phenomenon to constitutive equation

formulation, Scr. Mater. 170 (2019) 90–94. doi:10.1016/j.scriptamat.2019.05.040.
[12] G. Lee, E.A. Olevsky, C. Manière, A. Maximenko, O. Izhvanov, C. Back, J. McKittrick, Effect of electric current on densification behavior of conductive ceramic powders consolidated by spark plasma sintering, Acta Mater. 144 (2018) 524–533. doi:10.1016/j.actamat.2017.11.010.
[13] K.I. Rybakov, E.A. Olevsky, V.E. Semenov, The microwave ponderomotive effect on ceramic sintering, Scr. Mater. 66 (2012) 1049–1052. doi:10.1016/j.scriptamat.2012.02.043.
[14] E.A. Olevsky, A.L. Maximenko, E.G. Grigoryev, Ponderomotive effects during contact formation in microwave sintering, Model. Simul. Mater. Sci. Eng. 21 (2013) 055022. doi:10.1088/0965-0393/21/5/055022.
[15] R. Chaim, Electric field effects during spark plasma sintering of ceramic nanoparticles, J. Mater. Sci. 48 (2013) 502–510. doi:10.1007/s10853-012-6764-9.
[16] J. Narayan, A new mechanism for field-assisted processing and flash sintering of materials, Scr. Mater. 69 (2013) 107–111. doi:10.1016/j.scriptamat.2013.02.020.
[17] R. Chaim, C. Estournès, On thermal runaway and local endothermic/exothermic reactions during flash sintering of ceramic nanoparticles, J. Mater. Sci. 53 (2018) 6378–6389. doi:10.1007/s10853-018-2040-y.
[18] E.A. Olevsky, S. Kandukuri, L. Froyen, Consolidation enhancement in spark-plasma sintering: Impact of high heating rates, J. Appl. Phys. 102 (2007) 114913. doi:10.1063/1.2822189.
[19] W. Ji, B. Parker, S. Falco, J.Y. Zhang, Z.Y. Fu, R.I. Todd, Ultra-fast firing: Effect of heating rate on sintering of 3YSZ, with and without an electric field, J. Eur. Ceram. Soc. 37 (2017) 2547–2551. doi:10.1016/j.jeurceramsoc.2017.01.033.
[20] J. Zhang, F. Meng, R.I. Todd, Z. Fu, The nature of grain boundaries in alumina fabricated by fast sintering, Scr. Mater. 62 (2010) 658–661. doi:10.1016/j.scriptamat.2010.01.019.
[21] R. Chaim, Particle Surface Softening as Universal Behaviour during Flash Sintering of Oxide Nano-Powders, Materials (Basel). 10 (2017) 179. doi:10.3390/ma10020179.
[22] P.R. Cantwell, M. Tang, S.J. Dillon, J. Luo, G.S. Rohrer, M.P. Harmer, Grain boundary complexions, Acta Mater. 62 (2014) 1–48. doi:10.1016/j.actamat.2013.07.037.
[23] P.R. Cantwell, S. Ma, S.A. Bojarski, G.S. Rohrer, M.P. Harmer, Expanding time–temperature-transformation (TTT) diagrams to interfaces: A new approach for grain boundary engineering, Acta Mater. 106 (2016) 78–86. doi:10.1016/j.actamat.2016.01.010.
[24] R.K. Bordia, S.-J.L. Kang, E.A. Olevsky, Current understanding and future research directions at the onset of the next century of sintering science and technology, J. Am. Ceram. Soc. 100 (2017) 2314–2352. doi:10.1111/jace.14919.
[25] E.A. Olevsky, D. V. Dudina, Field-Assisted Sintering, Springer N, Springer International Publishing, Cham, 2018. doi:10.1007/978-3-319-76032-2.
[26] G.M. Jones, M. Biesuz, W. Ji, S.F. John, C. Grimley, C. Manière, C.E.J. Dancer, Promoting microstructural homogeneity during flash sintering of ceramics through thermal management, MRS Bull. 46 (2021) 59–66. doi:10.1557/s43577-020-00010-2.
[27] W. Qin, J. Yun, A.M. Thron, K. van Benthem, Temperature gradient and microstructure evolution in AC flash sintering of 3 mol% yttria-stabilized zirconia, Mater. Manuf. Process. 32 (2017) 1–8. doi:10.1080/10426914.2016.1232814.
[28] C. Manière, F. Borie, S. Marinel, Impact of convection and radiation on direct/hybrid heating stability of field assisted sintering, J. Manuf. Process. 56 (2020) 147–157. doi:10.1016/j.jmapro.2020.04.075.
[29] C. Manière, T. Zahrah, E.A. Olevsky, Inherent heating instability of direct microwave sintering process: Sample analysis for porous 3Y-ZrO2, Scr. Mater. 128 (2017) 49–52. doi:10.1016/j.scriptamat.2016.10.008.

[30] C. Manière, T. Zahrah, E.A. Olevsky, Fully coupled electromagnetic-thermal-mechanical comparative simulation of direct vs hybrid microwave sintering of 3Y-ZrO2, J. Am. Ceram. Soc. 100 (2017) 2439–2450. doi:10.1111/jace.14762.
[31] Y. Dong, On the Hotspot Problem in Flash Sintering, ArXiv. (2017) 1702.05565.
[32] S.H. Risbud, Y.-H. Han, Preface and historical perspective on spark plasma sintering, Scr. Mater. 69 (2013) 105–106. doi:10.1016/j.scriptamat.2013.02.024.
[33] C. Manière, L. Durand, E. Brisson, H. Desplats, P. Carré, P. Rogeon, C. Estournès, Contact resistances in spark plasma sintering: From in-situ and ex-situ determinations to an extended model for the scale up of the process, J. Eur. Ceram. Soc. 37 (2017) 1593–1605. doi:10.1016/j.jeurceramsoc.2016.12.010.
[34] C. Manière, A. Pavia, L. Durand, G. Chevallier, K. Afanga, C. Estournès, Finite-element modeling of the electro-thermal contacts in the spark plasma sintering process, J. Eur. Ceram. Soc. 36 (2016) 741–748. doi:10.1016/j.jeurceramsoc.2015.10.033.
[35] X. Wei, D. Giuntini, A.L. Maximenko, C.D. Haines, E.A. Olevsky, Experimental Investigation of Electric Contact Resistance in Spark Plasma Sintering Tooling Setup, J. Am. Ceram. Soc. 98 (2015) 3553–3560. doi:10.1111/jace.13621.
[36] A. Zavaliangos, J. Zhang, M. Krammer, J.R. Groza, Temperature evolution during field activated sintering, Mater. Sci. Eng. A. 379 (2004) 218–228. doi:10.1016/j.msea.2004.01.052.
[37] O. Vasylkiv, H. Borodianska, Y. Sakka, D. Demirskyi, Flash spark plasma sintering of ultrafine yttria-stabilized zirconia ceramics, Scr. Mater. 121 (2016) 32–36. doi:10.1016/j.scriptamat.2016.04.031.
[38] S. Grasso, T. Saunders, H. Porwal, O. Cedillos-Barraza, D.D. Jayaseelan, W.E. Lee, M.J. Reece, Flash Spark Plasma Sintering (FSPS) of Pure ZrB 2, J. Am. Ceram. Soc. 97 (2014) 2405–2408. doi:10.1111/jace.13109.
[39] S. Grasso, T. Saunders, H. Porwal, B. Milsom, A. Tudball, M. Reece, Flash Spark Plasma Sintering (FSPS) of α and β SiC, J. Am. Ceram. Soc. 99 (2016) 1534–1543. doi:10.1111/jace.14158.
[40] E.A. Olevsky, S.M. Rolfing, A.L. Maximenko, Flash (Ultra-Rapid) Spark-Plasma Sintering of Silicon Carbide, Sci. Rep. 6 (2016) 33408. doi:10.1038/srep33408.
[41] S. Grasso, E.-Y. Kim, T. Saunders, M. Yu, A. Tudball, S.-H. Choi, M. Reece, Ultra-Rapid Crystal Growth of Textured SiC Using Flash Spark Plasma Sintering Route, Cryst. Growth Des. 16 (2016) 2317–2321. doi:10.1021/acs.cgd.6b00099.
[42] E. Zapata-Solvas, S. Bonilla, P.R. Wilshaw, R.I. Todd, Preliminary investigation of flash sintering of SiC, J. Eur. Ceram. Soc. 33 (2013) 2811–2816. doi:10.1016/j.jeurceramsoc.2013.04.023.
[43] E. Castle, R. Sheridan, S. Grasso, A. Walton, M. Reece, Rapid sintering of anisotropic, nanograined Nd–Fe–B by flash-spark plasma sintering, J. Magn. Magn. Mater. 417 (2016) 279–283. doi:10.1016/j.jmmm.2016.05.067.
[44] R. McKinnon, S. Grasso, A. Tudball, M.J. Reece, Flash spark plasma sintering of cold-Pressed TiB 2 - h BN, J. Eur. Ceram. Soc. 37 (2017) 2787–2794. doi:10.1016/j.jeurceramsoc.2017.01.029.
[45] B. Niu, F. Zhang, J. Zhang, W. Ji, W. Wang, Z. Fu, Ultra-fast densification of boron carbide by flash spark plasma sintering, Scr. Mater. 116 (2016) 127–130. doi:10.1016/j.scriptamat.2016.02.012.
[46] M.M. Tünçay, J.A. Muñiz-Lerma, D.P. Bishop, M. Brochu, Spark plasma sintering and spark plasma upsetting of an Al-Zn-Mg-Cu alloy, Mater. Sci. Eng. A. 704 (2017) 154–163. doi:10.1016/j.msea.2017.08.015.
[47] H. Shang, A. Mohanram, E. Olevsky, R.K. Bordia, Evolution of anisotropy in hierarchical porous ceramics during sinter-forging, J. Eur. Ceram. Soc. 36 (2016) 2937–2945. doi:10.1016/j.jeurceramsoc.2015.12.042.
[48] E. Zapata-Solvas, D. Gómez-García, A. Domínguez-Rodríguez, R.I. Todd, Ultra-fast and energy-efficient sintering of ceramics by electric current concentration, Sci. Rep. 5

(2015) 8513. doi:10.1038/srep08513.
[49] B. Román-Manso, M. Belmonte, M.I. Osendi, P. Miranzo, Effects of Current Confinement on the Spark Plasma Sintering of Silicon Carbide Ceramics, J. Am. Ceram. Soc. 98 (2015) 2745–2753. doi:10.1111/jace.13678.
[50] C. Manière, G. Lee, E.A. Olevsky, All-Materials-Inclusive Flash Spark Plasma Sintering, Sci. Rep. 7 (2017) 15071. doi:10.1038/s41598-017-15365-x.
[51] E.A. Olevsky, Theory of sintering: from discrete to continuum, Mater. Sci. Eng. R Reports. 23 (1998) 41–100. doi:10.1016/S0927-796X(98)00009-6.
[52] E.A. Olevsky, C. Garcia-Cardona, W.L. Bradbury, C.D. Haines, D.G. Martin, D. Kapoor, Fundamental Aspects of Spark Plasma Sintering: II. Finite Element Analysis of Scalability, J. Am. Ceram. Soc. 95 (2012) 2414–2422. doi:10.1111/j.1551-2916.2012.05096.x.
[53] V.V. Skorohod, Rheological basis of the theory of sintering, Nauk. Dumka, Kiev. (1972).
[54] C. Manière, U. Kus, L. Durand, R. Mainguy, J. Huez, D. Delagnes, C. Estournès, Identification of the Norton-Green Compaction Model for the Prediction of the Ti-6Al-4V Densification During the Spark Plasma Sintering Process, Adv. Eng. Mater. 18 (2016) 1720–1727. doi:10.1002/adem.201600348.
[55] D. Martins, F. Grumbach, C. Manière, P. Sallot, K. Mocellin, M. Bellet, C. Estournès, In-situ creep law determination for modeling Spark Plasma Sintering of TiAl 48-2-2 powder, Intermetallics. 86 (2017) 147–155. doi:10.1016/j.intermet.2017.03.006.
[56] C. Manière, E.A. Olevsky, Porosity dependence of powder compaction constitutive parameters: Determination based on spark plasma sintering tests, Scr. Mater. 141 (2017) 62–66. doi:10.1016/j.scriptamat.2017.07.026.
[57] C. Manière, C. Harnois, S. Marinel, Porous stage assessment of pressure assisted sintering modeling parameters: a ceramic identification method insensitive to final stage grain growth disturbance, Acta Mater. 211 (2021) 116899. doi:10.1016/j.actamat.2021.116899.
[58] A. Pavia, L. Durand, F. Ajustron, V. Bley, G. Chevallier, A. Peigney, C. Estournès, Electro-thermal measurements and finite element method simulations of a spark plasma sintering device, J. Mater. Process. Technol. 213 (2013) 1327–1336. doi:10.1016/j.jmatprotec.2013.02.003.
[59] G. Molénat, L. Durand, J. Galy, A. Couret, Temperature Control in Spark Plasma Sintering: An FEM Approach, J. Metall. 2010 (2010) 1–9. doi:10.1155/2010/145431.
[60] C. Manière, T. Zahrah, E.A. Olevsky, Fluid dynamics thermo-mechanical simulation of sintering: Uniformity of temperature and density distributions, Appl. Therm. Eng. 123 (2017) 603–613. doi:10.1016/j.applthermaleng.2017.05.116.
[61] C. Manière, G. Lee, J. McKittrick, A. Maximenko, E.A. Olevsky, Graphite creep negation during flash spark plasma sintering under temperatures close to 2000 °C, Carbon N. Y. 162 (2020) 106–113. doi:10.1016/j.carbon.2020.02.027.
[62] C. Manière, G. Lee, E.A. Olevsky, Proportional integral derivative, modeling and ways of stabilization for the spark plasma sintering process, Results Phys. 7 (2017) 1494–1497. doi:10.1016/j.rinp.2017.04.020.
[63] U. Anselmi-Tamburini, S. Gennari, J.E. Garay, Z.A. Munir, Fundamental investigations on the spark plasma sintering/synthesis process, Mater. Sci. Eng. A. 394 (2005) 139–148. doi:10.1016/j.msea.2004.11.019.
[64] C. Maniere, A. Pavia, L. Durand, G. Chevallier, V. Bley, K. Afanga, A. Peigney, C. Estournès, Pulse analysis and electric contact measurements in spark plasma sintering, Electr. Power Syst. Res. 127 (2015) 307–313. doi:10.1016/j.epsr.2015.06.009.
[65] K. Vanmeensel, A. Laptev, J. Hennicke, J. Vleugels, O. Vanderbiest, Modelling of the temperature distribution during field assisted sintering, Acta Mater. 53 (2005) 4379–4388. doi:10.1016/j.actamat.2005.05.042.
[66] A. Van der Laan, V. Boyer, R. Epherre, C. Estournès, Simple method for the

identification of electrical and thermal contact resistances in spark plasma sintering, J. Eur. Ceram. Soc. 41 (2021) 599–610. doi:10.1016/j.jeurceramsoc.2020.08.073.
[67] J. Xu, Z. Liu, Z. Xie, S. He, X. Xi, DC electric field-assisted hot pressing of zirconia: methodology, phenomenology, and sintering mechanism, J. Am. Ceram. Soc. (2021) jace.17963. doi:10.1111/jace.17963.
[68] M.I. Mendelson, Average Grain Size in Polycrystalline Ceramics, J. Am. Ceram. Soc. 52 (1969) 443–446. doi:10.1111/j.1151-2916.1969.tb11975.x.
[69] C. Manière, G. Lee, J. McKittrick, S. Chan, E.A. Olevsky, Modeling zirconia sintering trajectory for obtaining translucent submicronic ceramics for dental implant applications, Acta Mater. 188 (2020) 101–107. doi:10.1016/j.actamat.2020.01.061.
[70] G. Guélou, C. Couder, C. Manière, C. Candolfi, B. Lenoir, L. Lallemant, C. Coureau, E. Guilmeau, Issues and opportunities from Peltier effect in functionally-graded colusites: From SPS temperature modeling to enhanced thermoelectric performances, Appl. Mater. Today. 22 (2021). doi:10.1016/j.apmt.2021.100948.
[71] G. Maizza, G.D. Mastrorillo, S. Grasso, H. Ning, M.J. Reece, Peltier effect during spark plasma sintering (SPS) of thermoelectric materials, J. Mater. Sci. 52 (2017) 10341–10352. doi:10.1007/s10853-017-1188-1.
[72] M. Biesuz, L. Pinter, T. Saunders, M. Reece, J. Binner, V. Sglavo, S. Grasso, Investigation of Electrochemical, Optical and Thermal Effects during Flash Sintering of 8YSZ, Materials (Basel). 11 (2018) 1214. doi:10.3390/ma11071214.
[73] J. Janek, Electrochemical blackening of yttria-stabilized zirconia â€“ morphological instability of the moving reaction front, Solid State Ionics. 116 (1999) 181–195. doi:10.1016/S0167-2738(98)00415-9.
[74] C. Manière, E. Torresani, E.A. Olevsky, Simultaneous spark plasma sintering of multiple complex shapes, Materials (Basel). 12 (2019). doi:10.3390/ma12040557.
[75] H. Hayashi, T. Saitou, N. Maruyama, H. Inaba, K. Kawamura, M. Mori, Thermal expansion coefficient of yttria stabilized zirconia for various yttria contents, Solid State Ionics. 176 (2005) 613–619. doi:10.1016/j.ssi.2004.08.021.

Figure captions

Figure 1 Flash SPS configuration, (a) 30 mm samples configuration and model boundary condition (b) mesh.

Figure 2 Calibration/verification of the electro-thermal-mechanical-microstructural simulation: (a) temperature curves, (b) temperature field of the SPS column, (c) grain size, (d) displacement, (e) specimen final relative density field, (f) simulated average relative density curve.

Figure 3 Temperature, displacement, rms current and voltage experimental data for the 30 mm tests, (a) die heating configuration 100 K/min, (b) die heating configuration 1000 K/min, (c) electric current concentration configuration (concentrated configuration) at 100 K/min, (d) electric current concentration configuration at 1000 K/min.

Figure 4 (a) Displacement and (b) simulated relative density curves, “dh” and “conc” refer to the “die heating” and “concentrated” configurations respectively.

Figure 5 Simulated ETMM model of the 15 mm diameter specimens in die heating configuration at 100 K/min and 1000 K/min.

Figure 6 Simulated ETMM model of the 15 mm diameter specimens in “concentrated” configuration at 100 K/min and 1000 K/min.

Figure 7 Simulated ETMM model of the 30 mm diameter specimens in die heating configuration at 100 K/min and 1000 K/min.

Figure 8 Simulated ETMM model of the 30 mm diameter specimens in “concentrated” configuration at 100 K/min and 1000 K/min.

Figure 9 Polished SEM microstructures of the specimens at 100 K/min, 1000 K/min and for the “die heating” and “concentrated” electrical current configurations.